

Provided for non-commercial research and education use.
Not for reproduction, distribution or commercial use.



This article appeared in a journal published by Elsevier. The attached copy is furnished to the author for internal non-commercial research and education use, including for instruction at the authors institution and sharing with colleagues.

Other uses, including reproduction and distribution, or selling or licensing copies, or posting to personal, institutional or third party websites are prohibited.

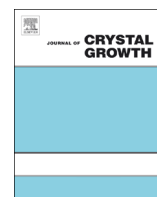
In most cases authors are permitted to post their version of the article (e.g. in Word or Tex form) to their personal website or institutional repository. Authors requiring further information regarding Elsevier's archiving and manuscript policies are encouraged to visit:

<http://www.elsevier.com/authorsrights>



Contents lists available at ScienceDirect

Journal of Crystal Growth

journal homepage: www.elsevier.com/locate/jcrysgr

Free energy of the bcc–liquid interface and the Wulff shape as predicted by the phase-field crystal model



Frigyes Podmaniczky^a, Gyula I. Tóth^a, Tamás Pusztai^a, László Gránásy^{a,b,*}

^a Institute for Solid State Physics and Optics, Wigner Research Centre for Physics, PO Box 49, H-1525 Budapest, Hungary

^b BCAST, Brunel University, Uxbridge, Middlesex UB8 3PH, UK

ARTICLE INFO

Available online 8 February 2013

Keywords:

A1. Solidification
A1. Surface energy anisotropy
A1. Wulff shape
A1. Phase-field crystal model

ABSTRACT

The Euler–Lagrange equation of the phase-field crystal (PFC) model has been solved under appropriate boundary conditions to obtain the equilibrium free energy of the body centered cubic crystal–liquid interface for 18 orientations at various reduced temperatures in the range $\epsilon \in [0, 0.5]$. While the maximum free energy corresponds to the {100} orientation for all ϵ values, the minimum is realized by the {111} direction for smaller ϵ (< 0.13), and by the {211} orientation for higher ϵ . The predicted dependence on the reduced temperature is consistent with the respective mean field critical exponent. The results are fitted with an eight-term cubic harmonic series, and are used to create stereographic plots displaying the anisotropy of the interface free energy. We have also derived the corresponding Wulff shapes that vary with increasing ϵ from sphere to a polyhedral form that differs from the rhombo-dodecahedron obtained previously by growing a bcc seed until reaching equilibrium with the remaining liquid.

© 2013 Elsevier B.V. All rights reserved.

1. Introduction

The anisotropy of the crystal–liquid interface free energy (γ_{hkl}) reflects differences in the interface structure for different orientations, and may play an essential role in determining the morphology of growing crystals [1]. Anisotropy is needed for dendritic structures, and apparently a detailed knowledge on anisotropy is required to fully understand the growth morphology [2]. Experimentally, the anisotropy of the interface free energy can be deduced from the shape of liquid inclusions in a solid matrix (though, one needs to be careful to relax all the stresses before converting the shape into anisotropy) [3–6]. Anisotropy has also been evaluated assuming that the dendrite growth directions correspond to the minima of the stiffness, and matching the minima of an appropriately parameterized interface stiffness function and the growth directions of dendrites observed in thin coatings [7]. Other methods evaluate the interface free energy and its anisotropy from molecular dynamics simulations [8–12] using empirical model potentials such as the embedded atom potential. Whether experiment [5–7] or atomistic simulation [8–12], the anisotropic interface free energy data are usually fitted by the cubic harmonic expansion series introduced by Fehlnner and Vosko

[13]. Often only a few low index orientations are considered (typically {100}, {110}, and {111}), and a second-order cubic harmonic expansion is employed [5–9].

Theoretical predictions for the anisotropy of the crystal–liquid interface in 3D emerge mostly from the early broken-bond models for the fcc, bcc, hcp, and dc structures [14–16] (utilizing former results for the crystal–vapor interfaces [17–21]), from the classical density functional theory [22,23], and recently for the fcc and bcc structures from the phase-field crystal (PFC) approach [23,24] (a simple dynamical density functional theory [25–27]). Some analytical predictions based on the approximations of the PFC model are also available: a multi-scale analysis has been used by Wu and Karma [28] to evaluate the anisotropy of the interfacial free energy near the critical point. They have approximated the equation of motion of the PFC model by a set of coupled equations that describe the time evolution of the amplitudes of the dominant density waves. Analyzing the stationary solution, they have concluded that the anisotropy is independent of the reduced temperature, a finding that accords with the results of Majaniemi and Provatas [29], who have used the local volume averaging method to obtain amplitude equations for liquid–solid interfaces that are broad relative to the periodicity of the crystal–line phase. In these studies, the independence of the anisotropy from the reduced temperature follows from approximations, which lead to weakly fourth-order amplitude theories of the Ginzburg–Landau type, from which all material parameters can be scaled out [28,29]. As a result, the anisotropy of the

* Corresponding author at: Institute for Solid State Physics and Optics, Wigner Research Centre for Physics, PO Box 49, H-1525 Budapest, Hungary. Tel.: +36 1 392 2222x3371.

E-mail address: Granasy.Laszlo@wigner.mta.hu (L. Gránásy).

solid–liquid interface free energy depends only on the crystal structure. This independence of the anisotropy from the reduced temperature is, however, unphysical, as the anisotropy must vanish, when the correlation length (the width of the solid–liquid interface) diverges at the critical point, as indeed suggested by the equilibrium shapes of finite size clusters from 2D PFC simulations [30–32]. It is, however, important to test the anisotropy of the solid–liquid interface free energy by equilibrium simulations for the flat interface in 3D, which is free from size effects, since the latter is known to influence the equilibrium shape considerably [21,30].

Accordingly, in this paper, we are going to demonstrate that the free energy of the flat bcc–liquid interface depends not only on the orientation but also on the reduced temperature. We map out the orientation dependence in detail at several reduced temperatures, then fit the results with an expression based on an eight-term Kubic harmonic expansion [13,33,34] to represent the orientation dependence in a closed form, and determine the respective Wulff shapes, a mathematical construction [17,35] to which the equilibrium shape, minimizing the interfacial contribution to the cluster free energy for a given volume, tends for large particle sizes.

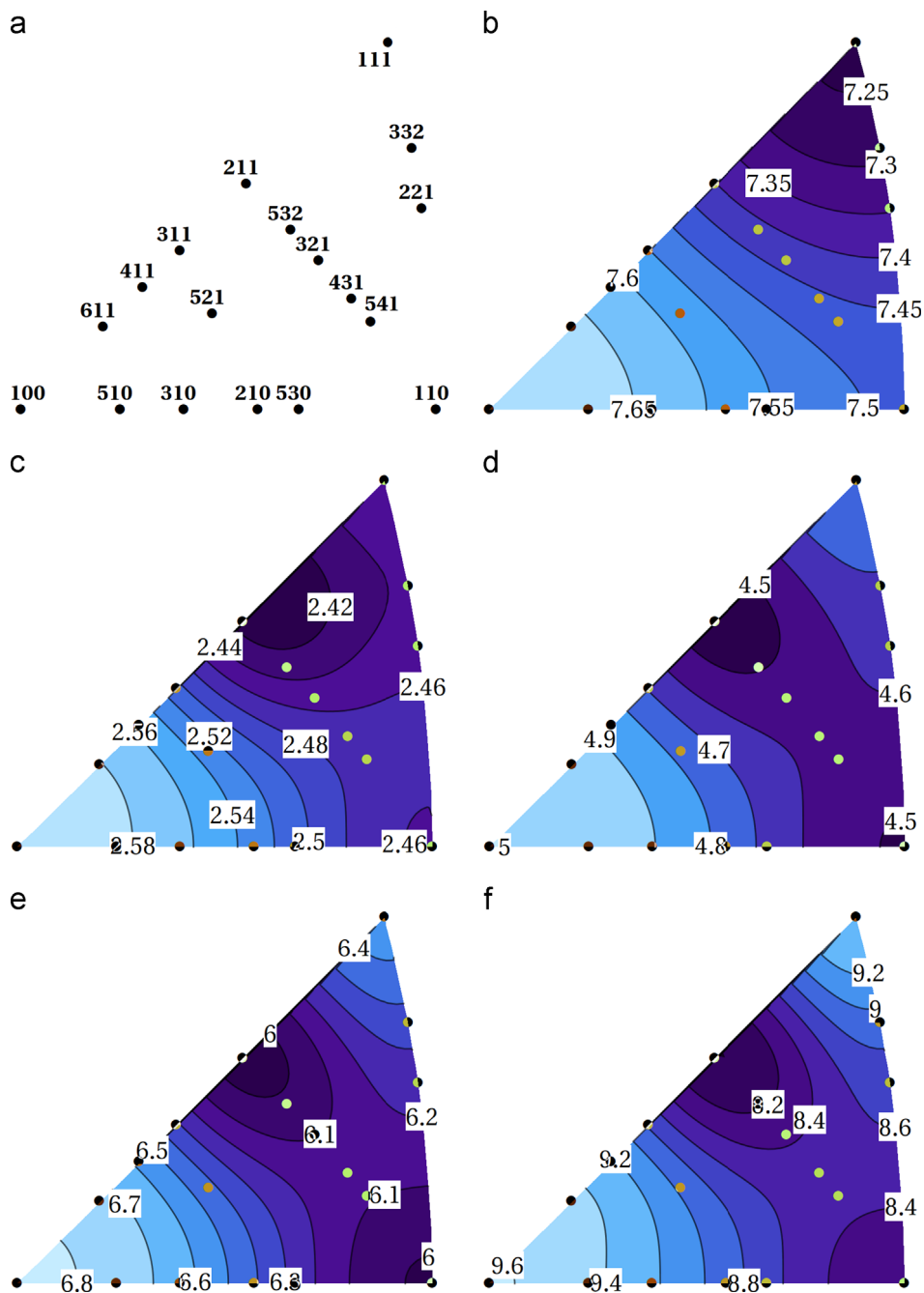


Fig. 1. Stereographic plots of the orientation dependence of the bcc–liquid interface free energy as a function of reduced temperature. The contour lines characterize the fitted Kubic harmonic expression. The 18 directions for which the interface free energy has been evaluated are shown in panel (a) and as inverted color dots in the other panels. Dimensionless γ_{hkl} values are shown, which has to be multiplied by the following factors: (b): 10^{-4} , (c)–(f): 10^{-3} . For panels (b)–(f), the reduced temperatures are $\epsilon = 0.1, 0.2, 0.3, 0.3748$ and 0.5 , respectively. (For interpretation of the references to color in this figure legend, the reader is referred to the web version of this article.)

2. The PFC model

In the PFC approach, the local state of matter is characterized by the time-averaged particle density, ρ . The dimensionless free energy of the inhomogeneous (crystal+fluid) system taken relative to a homogeneous reference fluid (of density $\rho_{L,ref}$) reads as

$$\Delta F = \int d\mathbf{r} \left\{ \frac{\psi}{2} [-\epsilon + (1 + \nabla^2)^2 \psi + \frac{\psi^4}{4}] \right\} \quad (1)$$

where $\psi \propto (\rho - \rho_{L,ref}) / \rho_{L,ref}$ is the scaled density difference. The reduced temperature ϵ can be connected to physical properties such as the bulk moduli of the fluid and crystalline phases at the reference density and temperature. Eq. (1) can be deduced [26,27] from the perturbative density functional theory of Ramakrishnan and Yussouff [36]. The solutions that extremize the free energy functional can be obtained by solving the respective Euler–Lagrange equation (ELE) [31]

$$\frac{\delta \Delta F}{\delta \psi} = \frac{\delta \Delta F}{\delta \psi} \Big|_{\psi_0} \quad (2)$$

where ψ_0 is the reduced particle density of the reference state, while a periodic boundary condition is assumed at the borders. Inserting the free energy functional into Eq. (2), rearranging then the terms, one obtains

$$[-\epsilon + (1 + \nabla^2)^2](\psi - \psi_0) = -(\psi^3 - \psi_0^3) \quad (3)$$

The ELE has been solved here numerically using a semi-spectral successive approximation scheme combined with the operator-splitting method [31,37]. The computations have been performed on 33 GPU units of total theoretical maximum computation rate of ~ 34.8 TFLOPS.

The free energy of the equilibrium solid–liquid interface has been determined in several steps: First, the equilibrium densities have been determined for the crystalline and liquid phases using the ELE method [31]. Then bcc–liquid–bcc sandwiches of equilibrium densities and of cross-section commensurable with the actual (hkl) face were created on which the ELE is solved using periodic boundary conditions. Next, the solution is inserted into the expression of grand-potential density and integrated (the contributions emerge exclusively from the interfacial regions), dividing then the result by twice the cross-sectional area, delivering the bcc–liquid interface free energy, γ_{hkl} , for the hkl orientation.

3. Results and discussion

First, we have determined γ_{hkl} for the 18 orientations shown in Fig. 1(a) for several reduced temperatures. Next, we have fitted an eight-term expression based on the Cubic harmonic expansion by Fehlner and Vosko [13] (Table 1) to the data (see the expansion coefficients and their standard deviation in Table 2).

The respective bcc–liquid interface free energy distributions are displayed as stereographic contour plots Fig. 1. Projection is applied from the north pole of the unit sphere to the perpendicular plane, touching the sphere at the south pole, which coincides with the 100 direction on the maps. Only the geodesic triangle spanned by the directions 100, 110 and 111 is shown, because of symmetry properties of the bcc structure. At low ϵ (< 0.13) the minimum and maximum directions are {111} and {100}, respectively. For larger ϵ the maximum direction remains the same, however, the minimum direction is {211}. The interface free energy for these low index directions are shown as a function of reduced temperature in Fig. 2. In agreement with the 2D results [31], the bcc–liquid data are consistent with the known mean-field critical exponent for the interface free energy (1.5). It is also clear that the anisotropy disappears as the critical point ($\epsilon = 0$) is approached. For comparison, we have plotted γ_{hkl} ($hkl=100, 110$, and 111) for the fcc–liquid interface at $\epsilon = 0.5, 0.65$, and 0.8 from Ref. [23].

Remarkably, the results for the two crystal structures are quite close. This is in accord with previous findings based on PFC nucleation data at $\epsilon = 0.3748$ [31], and with predictions from the nearest-neighbor broken-bond theory [14,15]. However, the closeness of the fcc–liquid and bcc–liquid interface free energies contradicts molecular dynamics simulations, which find that the bcc–liquid interface free energy is about 30% smaller than the data for the fcc–liquid interface [8–10]. A possible resolution of this contradiction could be that the MD simulations refer to metallic systems that would correspond to small ϵ values in the PFC model (where the interface is diffuse), whereas the PFC data of Ref. [23] for the fcc structure refer to very high ϵ values (where the interface is sharp and faceted, as in the case of the nearest-neighbor broken-bond model).

In approximating the Wulff shapes, first we have evaluated it directly from the 18 γ_{hkl} values (see Fig. 3). Accordingly, all physical information available for the system are accurately incorporated into the Wulff construction. We note that a small number of γ_{hkl} might be sufficient to describe a Wulff shape fully if the anisotropy is high (i.e. in the case of faceted crystals corresponding to high ϵ). However, the results are visually much less appealing if the anisotropy is low

Table 1
Terms $K_{j,k}$ of the Cubic harmonic expansion with a normalization by Fehlner and Vosko [13].

$K_{0,0} = 1$
$K_{4,1} = \frac{1}{4} \sqrt{21} [5Q - 3]$
$K_{6,1} = \frac{1}{8} \sqrt{\frac{13}{2}} [462S + 21Q - 17]$
$K_{8,2} = \frac{1}{32} \sqrt{561} [65Q^2 - 208S - 94Q + 33]$
$K_{10,2} = \frac{1}{64} \sqrt{\frac{455}{2}} [7106QS + 187Q^2 - 3190S - 264Q + 85]$
$K_{12,2} = \frac{3}{128} \sqrt{\frac{11}{41}} [2704156S^2 + 352716QS + 4199Q^2 - 232492S - 6526Q + 2423]$
$K_{12,3} = \frac{1}{128} \sqrt{\frac{676039}{246}} [1025Q^3 - 16212S^2 - 8532QS - 2298Q^2 + 4884S + 1677Q - 396]$
$K_{14,3} = \frac{15}{256} \sqrt{51765} [1311Q^2S + (437/18)Q^3 - (6992/3)S^2 - (7866/5)QS - (1577/30)Q^2 + (1501/3)S + (1109/30)Q - 17/2]$
$Q = n_x^4 + n_y^4 + n_z^4, S = n_x^2 n_y^2 n_z^2, \gamma(\mathbf{n}) = \sum C_{j,k} K_{j,k}$ and $\mathbf{n} = (n_x, n_y, n_z)$ is the unit direction vector

(non-faceted crystals occurring at low ϵ), since even the surfaces that should be smooth and rounded are covered by polygons [see e.g. Fig. 3(a), where a sphere is expected]. This is so, even if we use γ_{hkl} data for 18 independent orientations, a set that is far more numerous than usually obtained from experiments or molecular dynamics simulations.

This problem does not occur if we use the Kubic harmonic expression, as for any direction we may deduce γ_{hkl} . This comes, however, at a price. The γ_{hkl} data obtained from the fitted Kubic harmonic expression relies on eight expansion coefficients $C_{j,k}$ obtained from a fitting procedure, which are thus subject to errors. These errors are small if the anisotropy is low, but they

Table 2

Coefficients for the eight-term Kubic harmonic expansion normalized by the best fit isotropic contribution $\gamma_0 (= C_{0,0})$, together with their standard deviation.

ϵ	0.1	0.2	0.275	0.3	0.3748	0.5
γ_0	$7.494735E-04 \pm 4.40E-08$	$2.49173E-03 \pm 1.16E-06$	$4.12683E-03 \pm 5.59E-06$	$4.6828E-03 \pm 7.49E-06$	$6.3083E-03 \pm 1.44E-05$	$8.7469E-03 \pm 2.87E-05$
$C_{4,1}/\gamma_0$	$1.5373E-02 \pm 5.37E-05$	$2.0656E-02 \pm 4.24E-04$	$2.671E-02 \pm 1.24E-03$	$2.797E-02 \pm 1.46E-03$	$3.080E-02 \pm 2.08E-03$	$3.499E-02 \pm 3.00E-03$
$C_{6,1}/\gamma_0$	$-4.9062E-03 \pm 5.96E-05$	$-1.135E-03 \pm 4.71E-04$	$7.57E-03 \pm 1.37E-03$	$1.020E-02 \pm 1.62E-03$	$1.508E-02 \pm 2.31E-03$	$1.793E-02 \pm 3.33E-03$
$C_{8,2}/\gamma_0$	$-5.53E-04 \pm 5.38E-05$	$1.935E-03 \pm 4.25E-04$	$4.73E-03 \pm 1.24E-03$	$5.64E-03 \pm 1.47E-03$	$7.30E-03 \pm 2.08E-03$	$1.167E-02 \pm 3.00E-03$
$C_{10,2}/\gamma_0$	$-2.383E-04 \pm 4.74E-05$	$-4.497E-03 \pm 3.74E-04$	$-9.91E-03 \pm 1.09E-03$	$-1.125E-02 \pm 1.29E-03$	$-1.306E-02 \pm 1.83E-03$	$-1.890E-02 \pm 2.64E-03$
$C_{12,2}/\gamma_0$	$-7.92E-05 \pm 5.08E-05$	$-2.208E-03 \pm 4.02E-04$	$-4.14E-03 \pm 1.38E-03$	$-4.30E-03 \pm 1.38E-03$	$-4.795E-03 \pm 1.97E-03$	$-5.17E-03 \pm 2.84E-03$
$C_{12,3}/\gamma_0$	$-1.29E-05 \pm 4.63E-05$	$-1.498E-03 \pm 3.66E-04$	$-2.90E-03 \pm 1.07E-03$	$-3.19E-03 \pm 1.26E-03$	$-3.79E-03 \pm 1.79E-03$	$-6.86E-03 \pm 2.58E-03$
$C_{14,3}/\gamma_0$	$2.182E-04 \pm 5.05E-05$	$2.733E-03 \pm 3.99E-04$	$4.21E-03 \pm 1.16E-03$	$4.54E-03 \pm 1.38E-03$	$5.26E-03 \pm 1.96E-03$	$1.074E-02 \pm 2.82E-03$

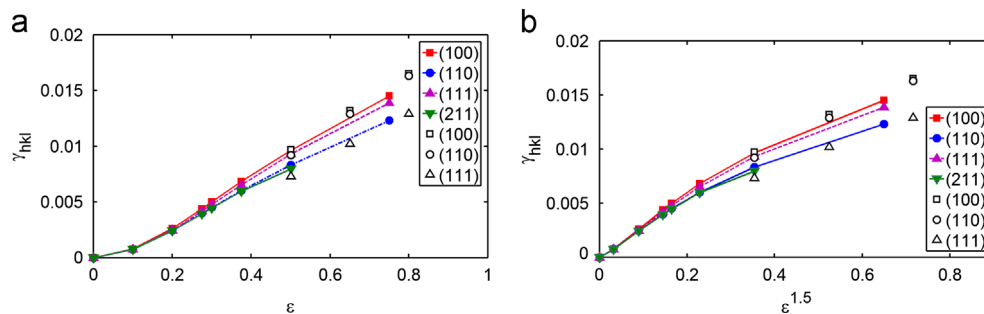


Fig. 2. (a) Bcc-liquid interface free energy (full symbols) vs. reduced temperature for a few low index orientations as predicted by the PFC model. (b) Interface free energy plotted vs. $\epsilon^{3/2}$. Note that the results are consistent with the mean-field critical exponent of the interface free energy. For comparison, data for the fcc-liquid interface from Ref. [23] are also shown (empty symbols). In contrast to the molecular dynamics results [8–10], the data for the fcc and bcc structures fall rather close to each other.

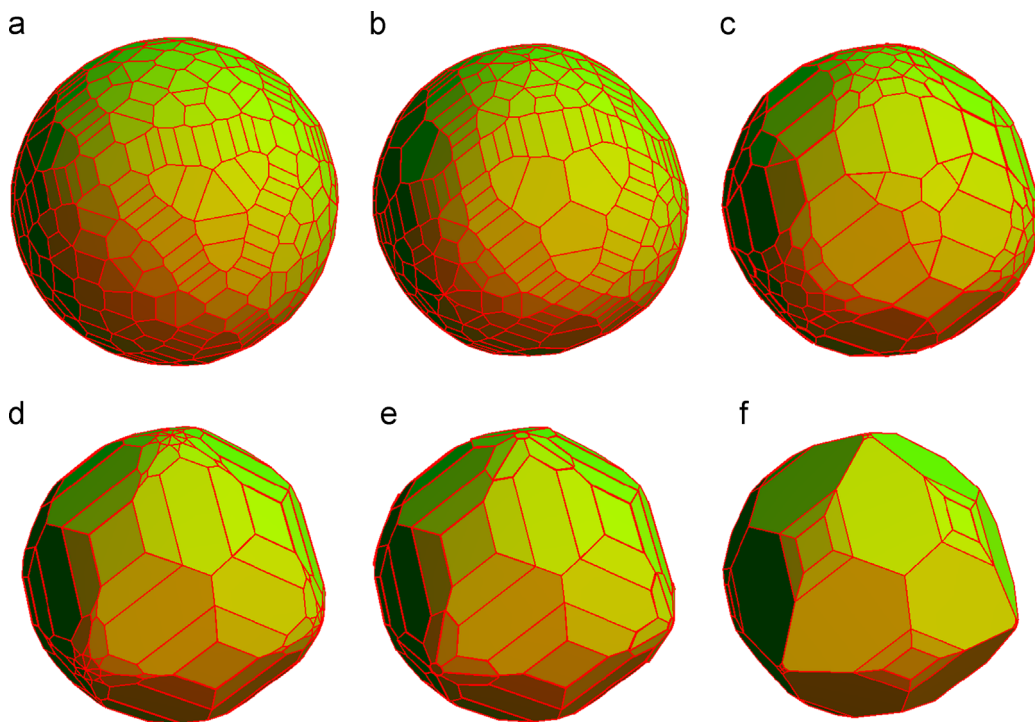


Fig. 3. Approximate Wulff shapes evaluated directly from the 18 γ_{hkl} data computed at the reduced temperatures $\epsilon = 0.0, 0.1, 0.2, 0.3, 0.3748,$ and $0.5,$ corresponding to panels (a)–(f), respectively.

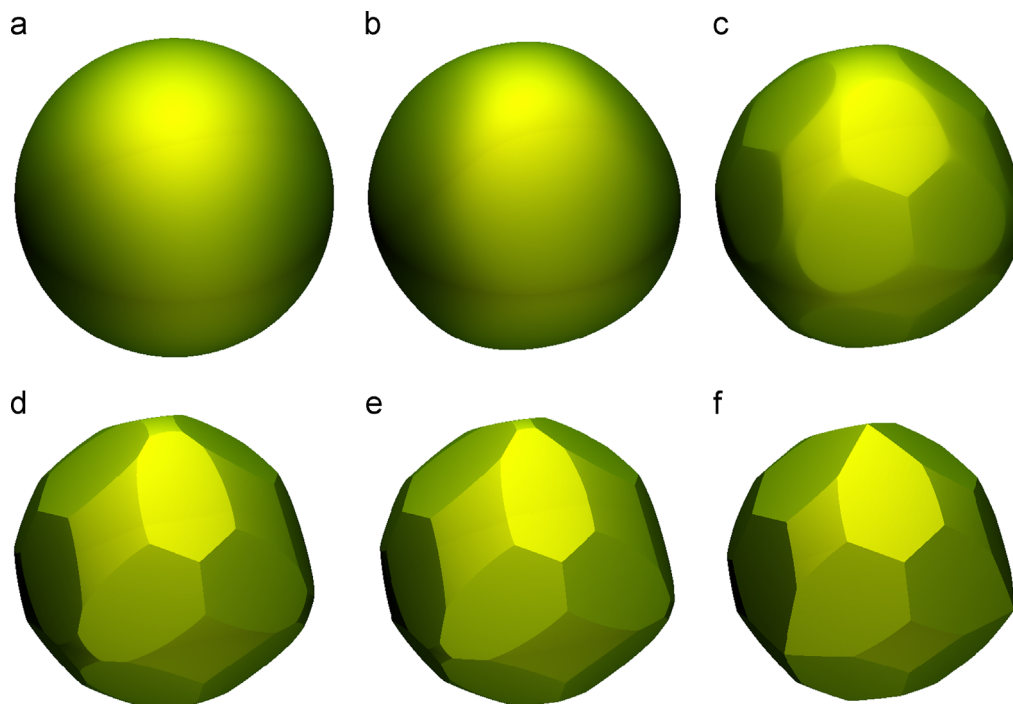


Fig. 4. Approximate Wulff shapes computed from the Kubic harmonic expressions (for the coefficients see Table 2) that were fitted to the 18 γ_{hkl} values evaluated at each reduced temperature ($\epsilon = 0.0, 0.1, 0.2, 0.3, 0.3748,$ and 0.5 for panels (a)–(f), respectively).

may be more significant if the anisotropy is high. Cusps in the polar plot of the interface free energy (γ -plot) might be especially problematic. These are the most important orientations, since often the γ value in these directions determines the whole Wulff shape. Unfortunately, the fit is expected to be the least accurate in the deepest cusps.

The approximate Wulff shapes emerging from this approach are displayed in Fig. 4. Indeed, the behavior for small ϵ is much improved, and we still obtain a fair reproduction for large anisotropies. This is supported by the fact that only small changes are seen if we merge the dense cover of orientations from the fitted Kubic harmonic expression with the originally computed γ_{hkl} data. However, still there are differences, which indicate that a large number of γ_{hkl} is needed to have a faithful representation of the orientation dependence of the interface free energy.

The Wulff shape changes from sphere at $\epsilon = 0$ to a polyhedral shape at large ϵ values. The latter shape differs considerably from the rhombo-dodecahedral form found by solving the PFC equation of motion for the growth of a bcc seed until reaching equilibrium with the remaining liquid [31,38]. The rhombo-dodecahedral shape obtained so (which has also been predicted by the nearest-neighbor broken-bond model as the Wulff shape for the bcc structure [14,17,35]) might be either the result of finite size effect or simply a growth form. Interestingly, the Wulff shapes found at large ϵ do not resemble the shapes observed experimentally for ^3He [39] or the equilibrium crystal shapes in vapor for metals [40]. In our study, the dominant faces are $\{110\}$ and $\{211\}$. Apparently, the $\{100\}$ faces have decreasing importance with increasing ϵ , whereas the $\{111\}$ face does not show up at all. These differences in the Wulff shape may be attributed to the fact that the Wulff shape is known to be sensitive to the interaction potential [18–20]. A recent work suggests that in the PFC model the effective pair-potential has a repulsive peak at $\approx r_0\sqrt{2}$, where r_0 is the radius corresponding to the main minimum of the potential [41], and this effective potential differs from the potentials expected for noble gases and metals. Further work is needed, however, to clarify whether the present Wulff

shapes are indeed consistent with such (Dzugutov-type [42]) interaction potential.

4. Summary

We have mapped the orientation and temperature dependence of the bcc–liquid interface free energy γ_{hkl} in the PFC model. As in 2D, the dependence of γ_{hkl} on the reduced temperature is consistent with the respective mean field exponent. A Kubic harmonic fit has been performed to represent the anisotropy. With increasing reduced temperature, the corresponding Wulff shape changes from sphere (at the critical point, $\epsilon = 0$) to a polyhedral shape at large ϵ that differs considerably from rhombo-dodecahedral, observed in dynamic simulations based on the PFC equation of motion.

Acknowledgement

This work has been supported by the EU FP7 Collaborative Project “EXOMET” (contract no. NMP-LA-2012-280421, co-funded by ESA), and by the ESA MAP/PECS projects “MAGNEPHAS III” (ESTEC Contract No. 4000105034/11/NL/KML) and “GRADE CET” (ESTEC Contract No. 4000104330/11/NL/KML).

References

- [1] J.J. Hoyt, M. Asta, A. Karma, Materials Science and Engineering Reports R 41 (2003) 121.
- [2] T. Haxhimali, A. Karma, F. Gonzales, M. Rappaz, Nature Materials 5 (2006) 660.
- [3] K.K. Koo, R. Ananth, W.N. Gill, Physical Review A 44 (1991) 3782.
- [4] A. Passerone, N. Eustathopoulos, Acta Metallurgica 30 (1982) 1349.
- [5] R.E. Napolitano, S. Liu, R. Trivedi, Interface Science 10 (2002) 217.
- [6] R.E. Napolitano, S. Liu, Physical Review B 70 (2004) 214103.
- [7] C. Niederberger, J. Michler, A. Jacot, Physical Review E 74 (2006) 021604.
- [8] M. Asta, C. Beckermann, A. Karma, W. Kurz, R. Napolitano, M. Plapp, G. Purdy, M. Rappaz, R. Trivedi, Acta Materialia 57 (2009) 941.
- [9] B.B. Laird, R.L. Davidchack, Journal of Physical Chemistry B 109 (2005) 17802.

- [10] D.Y. Sun, M. Asta, J.J. Hoyt, *Physical Review B* 69 (2004) 174103.
- [11] J.R. Morris, *Physical Review B* 66 (2002) 144104.
- [12] D.Y. Sun, M.I. Mendeleev, C.A. Becker, K. Kudin, T. Haxhimali, M. Asta, J.J. Hoyt, A. Karma, D. Srolovitz, *Physical Review B* 73 (2006) 024116.
- [13] W.R. Fehlner, S.H. Vosko, *Canadian Journal of Physics* 54 (1976) 2159.
- [14] L. Gránásy, M. Tegze, A. Ludwig, *Materials Science and Engineering A* 133 (1991) 577.
- [15] L. Gránásy, M. Tegze, *Materials Science Forum* 77 (1991) 243.
- [16] Q. Jiang, H.M. Lu, *Surface Science Reports* 63 (2008) 427.
- [17] G.A. Wolff, J.G. Gualtieri, *American Mineralogist* 47 (1962) 562.
- [18] J.K. Mackenzie, J.F. Nicholas, *Journal of Physics and Chemistry of Solids* 23 (1962) 185;
J.K. Mackenzie, J.F. Nicholas, *Journal of Physics and Chemistry of Solids* 23 (1962) 197.
- [19] J.F. Nicholas, *Australian Journal of Physics* 21 (1968) 21.
- [20] M. Dreschler, J.F. Nicholas, *Journal of Physics and Chemistry of Solids* 28 (1967) 2609.
- [21] L.D. Marks, *Surface Science* 150 (1985) 358.
- [22] W.B. Warshavsky, X. Song, *Journal of Physics: Condensed Matter* 22 (2010) 364112.
- [23] M. Oettel, S. Dorosz, M. Berghoff, B. Nestler, T. Schilling, *Physical Review E* 86 (2012) 021404.
- [24] H. Emmerich, H. Löwen, R. Wittkowski, T. Gruhn, G.I. Tóth, G. Tegze, L. Gránásy, *Advances in Physics* 61 (2012) 665.
- [25] K.R. Elder, M. Katakowski, M. Haataja, M. Grant, *Physical Review Letters* 88 (2002) 245701.
- [26] K.R. Elder, N. Provatas, J. Berry, P. Stefanovic, M. Grant, *Physical Review B* 75 (2007) 064107.
- [27] S. van Teeffelen, R. Backofen, A. Voigt, H. Löwen, *Physical Review E* 79 (2009) 051404.
- [28] K.-A. Wu, A. Karma, *Physical Review B* 76 (2007) 184107.
- [29] S. Majaniemi, N. Provatas, *Physical Review E* 79 (2009) 011607.
- [30] R. Backofen, A. Voigt, *Journal of Physics: Condensed Matter* 21 (2009) 464109.
- [31] G.I. Tóth, G. Tegze, T. Pusztai, G. Tóth, L. Gránásy, *Journal of Physics: Condensed Matter* 22 (2010) 364101.
- [32] G. Tegze, L. Gránásy, G.I. Tóth, J.F. Douglas, T. Pusztai, *Soft Matter* 7 (2011) 1789.
- [33] S.L. Altman, A.P. Cracknell, *Reviews of Modern Physics* 37 (1965) 19.
- [34] Fred C. Von der Lage, H.A. Bethe, *Physical Review* 71 (1947) 612.
- [35] G. Wulff, *Zeitschrift für Kristallographie und Mineralogie* 34 (1901) 449.
- [36] T.V. Ramakrishnan, M. Yussouff, *Physical Review B* 19 (1979) 2775.
- [37] G. Tegze, G. Bansel, G.I. Tóth, T. Pusztai, Z. Fan, L. Gránásy, *Journal of Computational Physics* 228 (2009) 1612.
- [38] G. Tegze, L. Gránásy, G.I. Tóth, F. Podmaniczky, A. Jaatinen, T. Ala-Nissila, T. Pusztai, *Physical Review Letters* 103 (2009) 035702.
- [39] H. Alles, A. Babkin, R. Jochemsen, A.Ya. Parshin, I.A. Todoshchenko, V. Tsepelin, *Proceedings of the National Academy of Sciences USA* 99 (2002) 1796.
- [40] Y. Saito, *Journal of Crystal Growth* 53 (1981) 273.
- [41] G.I. Tóth, T. Pusztai, G. Tegze, G. Tóth, L. Gránásy, *Physical Review Letters* 107 (2011) 175702.
- [42] J.P.K. Doye, D.J. Wales, F.H.M. Zetterling, M. Dzugutov, *Journal of Chemical Physics* 118 (2003) 2792.